From Electronic Structure to Ion Transport: Photoelectron Spectroscopy and Molecular Dynamics Simulations Reveal the Role of Anions in Lithium Battery Electrolytes

Journal:	*The Journal of Physical Chemistry*
Manuscript ID	jp-2025-03415p.R1
Manuscript Type:	Article
Date Submitted by the Author:	24-Jun-2025

Complete List of Authors:	Jiang, Yanrong; Shaoxing University, School of Mathematics Information Cao, Wenjin; Pacific Northwest National Laboratory, Physical Sciences Division Gao, Xiao-Fei; Pacific Northwest National Laboratory, Physical Sciences Division Zeng, Jinzhe; University of Science and Technology of China, School of Artificial Intelligence and Data Science Cao, Haoyu; Shaoxing University Zhu, Shunwei; Shaoxing University Wang, Wenhao; Shaoxing University Cheng, Xue; Shaoxing University Sun, Dongqin; Shaoxing University Chen, Feiyu; Shaoxing University Zhang, Weijia; Shaoxing University Hu, Zhubin; East China Normal University, State Key Laboratory of Precision Spectroscopy Wang, Xue-Bin; Pacific Northwest National Laboratory, Chemical & Materials Scienecs Division

From Electronic Structure to Ion Transport: Photoelectron Spectroscopy and Molecular Dynamics Simulations Reveal the Role of Anions in Lithium Battery Electrolytes

Yanrong Jiang[1, a], Wenjin Cao[2], Xiao-Fei Gao[2], Jinzhe Zeng[4, 5, 6], Haoyu Cao[1], Shunwei Zhu[1], Wenhao Wang[1], Xue Cheng[1], Dongqin Sun[1], Feiyu Chen[1], Weijia Zhang[1, *], Zhubin Hu[3, *], and Xue-Bin Wang[2,*]

[1] *School of Mathematics Information, Shaoxing University, Zhejiang 312000, China*

[2] *Physical Sciences Division, Pacific Northwest National Laboratory, 902 Battelle Boulevard, P.O. Box 999, Richland, Washington 99352, USA*

[3] *State Key Laboratory of Precision Spectroscopy, East China Normal University, Shanghai 200241, China*

[4] *School of Artificial Intelligence and Data Science, University of Science and Technology of China, Hefei 230026, China*

[5] *Suzhou Institute for Advanced Research, University of Science and Technology of China, Suzhou 215123, China*

[6] *Suzhou Big Data & AI Research and Engineering Center, Suzhou 215123, China*

*) Author to whom correspondence should be addressed: xuebin.wang@pnnl.gov; zbhu@lps.ecnu.edu.cn; zhangusx@yeah.net.

a) Email: yrjiang2017@163.com.

ABSTRACT:

Electrolyte anions are pivotal for lithium battery performance, yet their fundamental electronic structural properties are not well understood. In this work, we employ a combination of negative-ion photoelectron spectroscopy (NIPES), *ab initio* calculations, and molecular dynamics (MD) simulations to investigate the electronic structures of three representative electrolyte anions. This multi-scale approach enables us to elucidate how their intrinsic electronic properties govern anion–solvent interactions in gas-phase clusters, as well as lithium-ion (Li^+) solvation structures and ion transport behavior in the condensed phase. NIPES reveals that difluoro(oxalato)borate ($DFOB^-$), bis(fluorosulfonyl)imide (FSI^-), and bis(oxalato)borate (BOB^-) all exhibit high electron binding energies, with vertical/adiabatic detachment energies increasing from $DFOB^-$ (6.09/5.70 eV) to FSI^- (6.80/6.10 eV) to BOB^- (6.82/6.40 eV), correlating with enhanced oxidation stability. *Ab initio* calculations reveal that $DFOB^-$/FSI^-–solvent complexes bind Li^+ ~10 kcal/mol stronger than BOB^- series, aligning with strength of Li–anion model. $DFOB^-$ exhibits pronounced charge localization on both oxygen and fluorine atoms, enabling their involvement in Li^+ coordination. In contrast, fluorine atoms in FSI^- are largely electron-depleted and remain excluded from direct Li^+ binding. MD simulations further demonstrate that LiDFOB and LiFSI systems exhibit Li^+ diffusion coefficients three and five times higher than LiBOB across four common solvents. Notably, LiFSI salt in acetonitrile (AN) exhibits the fastest Li^+ diffusion among twelve electrolyte system, highlighting the synergistic effect of FSI^- and AN in promoting ion mobility. These findings provide a molecular-level understanding of the critical roles of anion and its micro-solvation in optimizing Li^+ diffusion dynamics, once again emphasizing the positioning FSI^- and $DFOB^-$ as prime candidates for next-generation electrolytes.

Ⅰ. INTRODUCTION

Lithium-ion batteries (LIBs) have become the cornerstone of modern energy storage technologies, driving applications ranging from portable electronics to electric vehicles and grid-scale renewable integration.[1] As battery systems evolve toward higher voltage cathodes[2-4] (e.g., NCM811, LNMO), silicon-based anodes,[5-6] and even lithium metal architectures,[7-9] conventional electrolyte formulations based on $LiPF_6$ in carbonate solvents are increasingly unable to meet the demands of stability, efficiency, and longevity under harsh operating conditions.[10-11] Central to the advancement of next-generation LIBs is the rational design of electrolytes that can achieve high ionic conductivity, wide electrochemical stability windows, and robust interfacial compatibility,[12-15] which are meticulously tailored to specific cell chemistries. Among various components, the choice of lithium salt—particularly its anion—is a key determinant of electrolyte performance.[16-17] Anions in electrolyte recipes, in particular, not only govern the solvation structure around Li^+ but also influence critical phenomena such as desolvation kinetics, solid or cathode electrolyte interphases (SEI/CEI) formation, and dendrite suppression through strong cation–anion interactions.[16, 18-22]

These macroscopic properties, along with microscopic solvent structures and interfacial dynamics, are closely tied to the intrinsic electronic structural properties of anions. Recent progress has seen growing interest in alternative lithium salts featuring multifunctional anions, such as bis(fluorosulfonyl)imide (FSI^-), difluoro(oxalato)borate ($DFOB^-$), bis(oxalato)borate (BOB^-).[23-25] Especially, the $DFOB^-$/FSI^- anions have demonstrated superior thermal and oxidative stabilities, as well as enhanced ability to form robust LiF-rich SEI interphases.[26-32] Previous studies have emphasized the multifaceted roles of anions in LIB electrolytes, including their impact on interfacial stability, solvation structures, and safety enhancement.[17, 33] Several investigations further suggest that anions may directly integrate into the Li^+ solvation shell, modulating

solvation dynamics and desolvation energetics through non-covalent interactions such as hydrogen bonding or dipole-dipole coupling, particularly via the proposed "lithium bond" framework.[34-37] And the lithium bond (Li bond) proposed by Zhang et al. was clarified by the down shift of ^{7}Li chemical shift,[34] which indicates an electron localization effect of the Li bond beyond electrostatic interactions. However, a fundamental understanding of the intrinsic electronic structural properties of these anions and the specific mechanisms at molecular level governing these effects—especially the interplay between anion chemistry, solvation coordination, and ion transport kinetics—remains elusive. And four functional solvents were specifically selected to elucidate the critical role of anion-induced interactions in governing ion transport mechanisms, including acetonitrile (AN), ethylene carbonate (EC), butyl acrylate (BA), and fluoroethylene carbonate (FEC). EC and FEC are well-established electrolyte components that are used in commercial LIBs. AN has also been found to have high oxidative stability and high ionic conductivity, enabling it to be as a promising candidate for electrolyte.[38] Furthermore, the inclusion of the novel organic solvent BA was motivated by its demonstrated ability to enhance low-temperature ionic conductivity.[39]

In this work, we report a photoelectron spectroscopy study of three promising anions (BOB^-, $DFOB^-$, FSI^-) using cryogenic NIPES. This experimental approach provides direct insight into their intrinsic electronic structures, including vertical (VDEs) and adiabatic electron detachment energies (ADEs), thereby establishing a foundational basis for comparing their redox behaviors. Complemented by quantum chemistry calculations on gas-phase Li^+–anion–solvent clusters, we elucidate how the distinct electronic structures of these anions govern their interactions with solvent molecules and Li^+ ions. Charge distribution analysis reveals that fluorine (F) atoms in FSI^- barely participate in the Li^+ coordination in the condensed phase, whereas the electron-enriched F atoms in $DFOB^-$ exhibit partial coordination ability across various solvents. To quantify the strength of anion-mediated Li bond interactions, a ternary 1:1:1 Li^+–anion–solvent cluster

model is proposed, linking anion-specific binding motifs to Li^+ diffusion behavior. Furthermore, symmetry-adapted perturbation theory (SAPT) analyses offer mechanistic insights into the nature of intermolecular interactions within these systems. MD simulations provide critical insights into the dynamic behavior of anion and the decisive role in determining self-diffusion coefficients across twelve electrolytes. Coordination structure analysis further reveals that the composition and geometry of the Li^+ solvation shell are strongly anion-dependent. Overall, investigating the fundamental electronic structures of anions provides critical insights into the molecular-level mechanisms connecting anion physicochemical properties, Li^+ solvation structures, and ion transport kinetics, thereby offering a guiding framework for the rational design of high-performance electrolytes for advanced lithium batteries.

Ⅱ. EXPERIMENTAL AND THEORETICAL METHODS

A. Negative ion photoelectron spectroscopy. The NIPES experiments were conducted using an integrated apparatus consisting of an electrospray ionization (ESI) source, a cryogenic three-dimensional ion trap and a magnetic bottle time-of-flight (TOF) photoelectron spectrometer.[40] An ~ 0.1 mM acetonitrile solution of each lithium salts (LiBOB, LiDFOB, LiFSI) was prepared and sprayed to generate the corresponding anions. All the anions were guided through two radiofrequency quadrupoles, a 90° ion deflector, and transferred into the cryogenic ion trap (set at 20 K), where they were accumulated and cooled by collisions with a cold buffer gas (20% H_2 balanced in helium) for 20 to100 ms. The cryogenically cooled anions were subjected to mass selection by a TOF mass spectrometer and then decelerated prior to photodetachment using 157 nm (7.866 eV) photons from an F_2 excimer laser, operated at a 20 Hz repetition rate with the anion beam off at alternating laser shots to afford shot-to-shot background subtraction. The resulting photoelectrons were collected with nearly 100% efficiency by the magnetic bottle and analyzed with a 5.2 m long electron flight tube. Recorded flight times were converted into kinetic energies calibrated using the known spectra of I^-/$Au(CN)_2^-$.[41-42]

The electron binding energy (eBE) spectra were obtained by subtracting the electron kinetic energies from the detachment photon energy with an electron energy resolution ($\Delta E/E$) of ~ 2% (i.e., ~20 meV for 1 eV kinetic energy electrons).

B. Quantum chemical calculations. This study examines four fundamental paired interactions in electrolyte systems: Li^+–anion, Li^+–solvent, anion–solvent and Li^+–(anion–solvent) (anion = BOB^-, $DFOB^-$, FSI^-; solvent = AN, EC, BA, FEC). To explore the essential characteristics and intensities of these paired interactions in the gas phase, a series of gradient-based optimization methods were utilized to identify the global minima and low-lying isomers of the corresponding four cluster types mentioned above. And this configuration search methodology has been validated by our previous work.[43-44] Hundreds of thousands of initial configurations were generated by Molclus code[45] and screened through the optimization energy calculated by the semi-empirical GFN2-xTB[46-47] method until the self-developed energy and configuration deviation convergence standard was reached. The retained isomers were then screened by an optimization filter performed by r2SCAN-3c method embedded in ORCA 5.0.4 codes.[48] Another round of single point energy and optimization filter was carried out using the ωB97X-2[49]/ma-def2-TZVP and ωB97XD[50]/aug-cc-pVTZ[51] methods with Grimme's dispersion corrections,[52-53] respectively. The final sorting rule for low-lying isomers was determined by the 20 K Gibbs free energy, computed using the DLPNO-CCSD(T)[54-55] electronic energy and ωB97XD/aug-cc-pVTZ thermal correction energy at 20 K with a 0.975 scaled factor for zero-point energy.[56] The vibrational frequencies were computed to confirm that final sorted isomers corresponded to stationary points on the potential energy surface. Theoretical VDEs for isolated anions and the corresponding anion–solvent cluster systems were calculated as the energy difference between neutral radicals ($A^{\cdot}$) and anionic (A^-) states, based on anions' optimized geometries. Six representative levels of theory test methods (i.e., PBE0,[57] B3LYP,[58] M06-2X,[59] DLPNO-CCSD(T), IP-EOM-DLPNO-CCSD[60] and ωB97XD) were tested to benchmark the experimental VDEs (Table

S1). The root mean square errors (RMSEs) of computed VDEs against the experimental values are 0.15 and 0.34 eV for ωB97XD and IP-EOM-DLPNO-CCSD methods,[60] respectively, rendering them both suitable methods for theoretically characterizing photodetachment processes. The symmetry-adapted perturbation theory (SAPT) at the SAPT2+[61-62]/aug-cc-pVDZ level was further applied to decompose the inner nature of binding energies (BEs) in Li^+–anion, Li^+–solvent, anion–solvent and Li^+–(anion–solvent) (anion = BOB^-, $DFOB^-$, FSI^-; solvent = AN, EC, BA, FEC) systems using the PSI4 code.[63] For Li^+–(anion–solvent) systems, the Li bond energy was defined as the interaction energy between Li^+ ion and the entire anion–solvent complex. The plots of highest occupied molecular orbitals (HOMOs) and independent gradient model based on Hirshfeld partition (IGMH) were generated by Multiwfn software[64] and rendered by VMD program.[65] All density functional theory (DFT) calculations were carried out using the Gaussian 16 software,[66] except where ORCA software was emphasized. The complex cluster structures discussed in the main text are all based on the most stable configurations identified through our search methodology. And the details about the energy threshold and retained structures in each step for the Li^+-anion-solvent cluster conformation search are presented in Table S2.

C. Force-field molecular dynamics simulations. MD simulations were performed using GROMACS 2020.2 code[67] for 1.0 M electrolytes of LiBOB, LiDFOB, LiFSI in AN, EC, BA and FEC, respectively. General Amber force fields (GAFF) parameters[68] were used for all the solvent molecules and anions, while boron atom used the Universal force field (UFF).[69] The Lennard-Jones (LJ) parameters for lithium cation were taken from literatures.[70-72] The fitting restrained electrostatic potential ($RESP2_{0.5}$) charges were computed by Multiwfn code[24] employing the ωB97XD/aug-cc-pVTZ method. And the widely applied[73-75] $RESP2_{0.5}$ charges that have taken into account the mean charges in solvent and gas phase to reasonably consider the polarization effect using standard two-stage fitting procedure (Table S3) were employed. Each electrolyte formulation consisted

of 75 lithium salt molecules dissolved in solvents of varying experimental densities, 1441 for AN, 1129 for EC, 525 for BA and 1032 for FEC. The molecules were initially packed randomly in a periodic cubic box of size 50 × 50 × 50 Å^3 using PACKMOL.[76] After the whole system energy minimization with a conjugate gradient algorithm, the system was then gently heated from 0 to 298.15 K in 100 ps in the canonical ensemble (NVT) and then equilibrated for another 2 ns. A pre-production run of 60 ns was conducted under constant temperature and pressure setting (constant NPT) with the temperature coupled to the V-rescale[77] thermostat at 298.15 K and the pressure referenced to 1 bar using Berendsen[78] pressure coupling. The simulation cubic box adjusted dynamically in response to pressure fluctuations under NPT conditions (Table S4). The coupling constants for temperature and pressure were set to 0.2 and 2.5 ps, respectively, with a compressibility of 4.5 × 10^{-5} bar^{-1}. For hydrogen bonded systems, bonds involving H-atoms were constrained with the LINCS[79] algorithm. The cut-off radii for Coulomb and van der Waals interactions were both 10 Å. Long-range corrections of electrostatics were handled by the PME[80] method. The system was initialized with a Maxwell velocity distribution at 298.15 K, and a time step of 1 fs was used throughout the simulations. Finally, a 60 ns production run was conducted under canonical ensemble to simulate the diffusion traits of electrolytes. Except for the absence of pressure coupling, all other parameters in NVT remained consistent with the settings of the NPT pre-production run. A stable 10 ns out of 60 ns NVT production run was analyzed for quantitative characterization of the configurational structure and ion transport behavior with V-rescale thermostat at 298.15 K. Based on the force field and dynamics simulations, the calculated diffusion coefficients of Li^+ and FSI^- anion in LiFSI-EC electrolyte were 0.4 and 0.6 × 10^{-10} m^2 s^{-1}, respectively, which exhibit qualitative consistency with the experimental measurements of 0.16 and 1.64 × 10^{-10} m^2 s^{-1} reported by Johannes et al.[81] The quantitative discrepancies arise from inherent limitations in classical force fields (e.g., oversimplified charge distribution models and neglect of polarization effects), while the

semi-quantitative agreement validates the reliability of our MD framework for probing ion transport mechanisms.

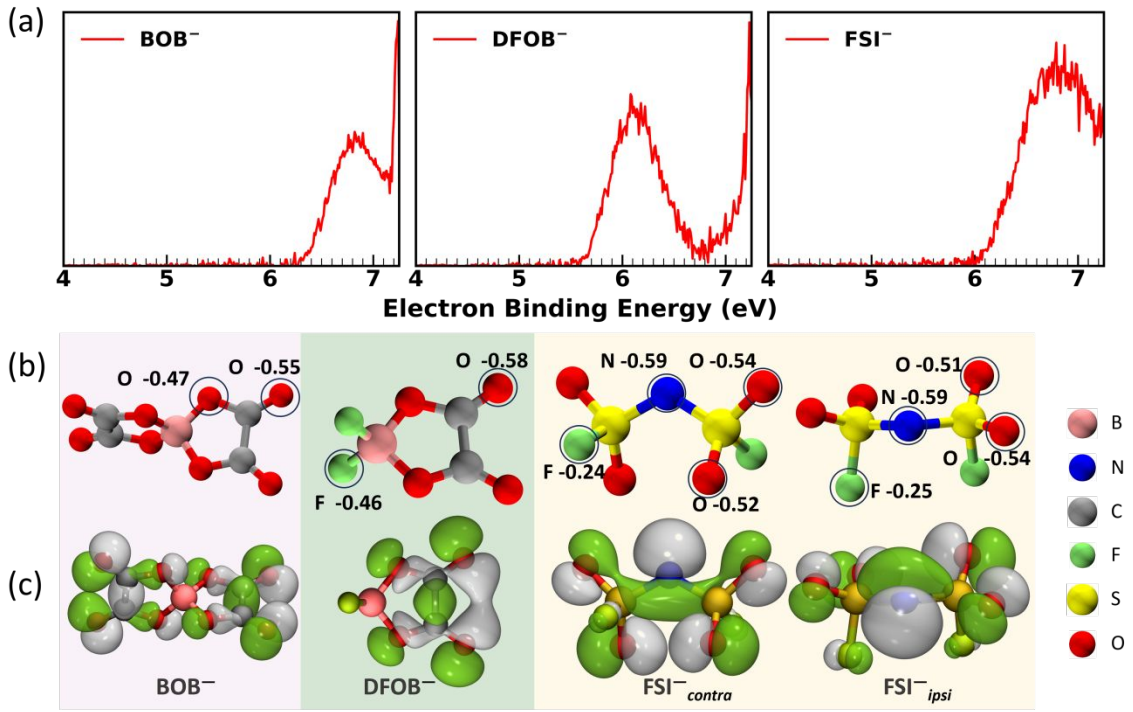

Figure 1. (a) Measured 20 K NIPE spectra of BOB^-, $DFOB^-$ and FSI^- photodetached by 157 nm photons. (b) RESP charges on selected atoms of BOB^-, $DFOB^-$, FSI^-_{contra} and FSI^-_{ipsi} anions. (c) HOMO plots. The ball-stick models with B, N, C, F, S, and O atoms are in pink, blue, gray, green, yellow, and red, respectively.

Ⅲ. RESULTS AND DISCUSSIONS

A. Electron Binding Energies and Gas/Solution Phase Oxidation. The oxidation resistance of electrolytes is of paramount importance, particularly in the context of high operating voltages, which are critical for enhancing the energy density of LIBs (typically > 4.2 V). NIPE spectra has been verified as a tool to predict the absolute oxidation potential of anion (A^-).[40] The measured ADE/VDE values reflect the difficulty of removing electrons adiabatically or vertically from anions and are inherently correlated with the solution phase redox potentials (E^o_{abs} (A^-)) of anion (A^-), according to the equation (1).

When approximating dissolution free energy of neutral radicals ($A^{\cdot}$) and anionic (A^{-}) states ($\Delta G^{o}_{(s)}(A^{\cdot}) - \Delta G^{o}_{(s)}(A^{-})$) as a constant among the studied anions and neglecting thermal corrections ($T\Delta S$), gas-phase ADEs can reasonably predict absolute oxidation potential trends. When the process is further approximated to vertical, the VDEs also become predictive. F is the Faraday constant.

$$E^{o}_{abs}\,(A^{-}) = \left[ADE(VDE) - T\Delta S + \Delta G^{o}_{(s)}(A^{\cdot}) - \Delta G^{o}_{(s)}(A^{-})\right]/(1)$$

Table 1. Experimental and calculated vertical/adiabatic detachment energies (VDEs/ADEs) and the absolute adiabatic oxidation energy (E^{o}_{abs}) of anions in four solvents (in eV).

		BOB^{-}		$DFOB^{-}$		FSI^{-}_{contra}/ FSI^{-}_{ipsi}	
		Exp.[a]	Cal.[b]	Exp.	Cal.	Exp.	Cal.
isolated	VDE	6.82	6.74 (7.08)	6.09	6.02 (6.31)	6.80	6.69 (6.83) / 6.43 (6.62)
	ADE	6.40	5.98	5.70	5.25	6.10	5.58 / 5.62
AN	E^{o}_{abs}[c]		7.83		7.61		7.98
EC			7.83		7.62		7.98
BA			7.61		7.29		7.64
FEC			7.84		7.62		7.98

[a] Experimental VDE/ADE uncertainty ± 0.1 eV; [b] calculated VDEs/ADEs using the ωB97XD and IP-EOM-DLPNO-CCSD methods (the latter are shown in parentheses) with the aug-cc-pVTZ basis set; [c] absolute adiabatic oxidation energy (E^{o}_{abs}) of anions in four solvents derived from equation 1 based on experimental ADEs and dissolution free energy employing SMD solvation model.

Figure 1(a) shows the 20 K NIPE spectra of BOB^{-}, $DFOB^{-}$ and FSI^{-}. All three type anions have extremely high electron binding energies. The experimental VDEs and ADEs are determined from the position of the first spectral maximum and spectral onset,

respectively. As listed in Table1, the measured VDEs and ADEs for FSI^- (6.80, 6.10 eV) and BOB^- (6.82, 6.40 eV) exceed that of $DFOB^-$ (6.09, 5.70 eV), underscoring their relatively strong intrinsic oxidation stability. The calculated VDEs at the level of ωB97XD and IP-EOM-DLPNO-CCSD/aug-cc-pVTZ method accurately reproduced the experiment VDEs. Although the calculated ADEs are ~0.46 eV lower than the experimental ones on average, the trend of the experimental ADEs was well reproduced. This numerical difference between experimental and calculated ADEs can be related to the significant structural changes of the neutral radicals ($A^{\cdot}$) compared to the anions (A^-) (Figure S1). The calculated ADE involves the 0–0 transition in the vibrational ground state, while the measured ADE refers to a not fully relaxed state of the neutral and should be regarded as an upper limit of the true ADE. Moreover, the VDE trends correlate with the highest occupied molecular orbital (HOMO) energies (-6.4 eV for BOB^-, -5.6 eV for $DFOB^-$, and -6.4 eV for FSI^-), highlighting the interplay between electronic structure and intrinsic redox stability.

Two isomers of FSI^- are identified show in Figure 1(b). The lowest-energy isomer (FSI^-_{contra}) with C_2 symmetry exhibits fluorine atoms in a contralateral configuration, while the second-lowest-energy isomer (FSI^-_{ipsi}), with fluorine atoms in an ipsilateral arrangement, is higher in energy by 1.11 kcal/mol. This energy difference was computed using DLPNO-CCSD(T)/aug-ccc-pVTZ electronic energies and ωB97XD/aug-ccc-pVTZ thermal corrections at 20 K. The calculated VDEs of FSI^-_{contra} and FSI^-_{ipsi} are 6.83 eV and 6.62 eV, respectively, as determined using IP-EOM-DLPNO-CCSD/aug-cc-pVTZ. These two close-lying isomers with certain differences in VDEs are likely coexist in the experiments, leading to a slightly broader spectral band of FSI^- compared to other two electrolyte anions. And the minor energy differences reflect similar charge distributions and HOMO localization across the N-S rotated isomers. As shown in Figure 1c, the HOMO populations indicate electron removal primarily from O and N atoms rather than from F atoms in both FSI^- isomers. In contrast, $DFOB^-$ exhibits pronounced negative

charge localization on its fluorine atoms, although these minimally contribute to the HOMO, akin to FSI^-. However, the electro-enriched fluorine atoms at the endpoint of $DFOB^-$ can facilitate its participation in the Li^+ solvation shell of LiDFOB-BA electrolyte in following MD analysis (Figure 5b). Electrostatic potential (ESP) maps provided in Figure S2 indicate a pronounced negative charge region around the fluorine atoms, providing a favorable environment for electrostatic interactions with Li^+. BOB^- and FSI^- distribute negative charges across the four oxygen atoms at their endpoints, all of which contribute to the HOMO and participate in the coordination of Li^+ solvation shell. These detailed analyses of anionic electronic structures provide critical insights into the effect of anions on microscopic structure of the Li^+ solvation shell.

Moreover, the solvent environment significantly affects the electronic structure of anions (A^-), as well as the corresponding solution phase oxidation potential E^o_{abs} (A^-). According to equation 1, we provide the quantitative data of E^o_{abs} (A^-) for all three anions in four solvents to predict solvation effect, as shown in Table 1 and Figure 2(a). The calculated E^o_{abs} (A^-) incorporates a measured ADE, an entropic term ($-T\Delta S$) computed using ωB97XD/aug-cc-pVTZ method at 298.15 K, and the respective anion and neutral solvation free energies derived from solvation model based on density (SMD) calculated at the M052X/6-31G(d) level, which is suitable for calculating solvation free energy.[82] And the trend of calculated E^o_{abs} (A^-) in different solvent in Table 1 and Figure 2(a) aligns with the trend of calculated VDEs of anion-solvent cluster models listed in Table S5. This indicates that electronic structure stability of anion–solvent cluster allows rational prediction of solvent effects on anion oxidation stability in solution phase.

In anion–solvent cluster model, BA solvent yields smallest VDE shift from the isolated anion among four tested solvents (Table S5). This aligns with the predicted lowest E^o_{abs} of three anions in BA solvent due to the BA lowest dielectric constant (ε = 5.25). As reported previously, low dielectric constant solvents minimally enhance oxidative stability. And increasing the dielectric constant beyond a threshold does not

proportionally improve oxidative stability.[83] EC (ε = 95.3) and FEC (ε = 102) solvent show similar oxidative stability to AN (ε = 36.6) for the anions, as listed on Table 1. This slightly deviates from the trend predicted by the anion–solvent cluster model (Table S5), potentially because the model is more sensitive to anion-solvent interactions in small cluster size regime. In Table S5, the average VDEs of the three anions in mono-EC/FEC-solvated clusters are ~0.2 eV higher than those in AN, but the former two VDEs in EC/FEC are nearly identical. This observation is consistent with the uniform enhancement in oxidative potential attributed to the implicit solvation effects of these solvents. Both models can reasonably predict that AN, EC and FEC solvents can effectively enhance oxidation stability.

By analyzing the specific interactions between an anion and a solvent molecule with cluster model, we can elucidate the essence of the underlying mechanism leading to the enhanced oxidation stability. The increasing trend of VDEs in Table S5 aligns with interaction energies calculated by SAPT2+/aug-cc-pVDZ method (Table S6). The weak interactions between the FSI^- anion and solvent molecules are all below 19 kcal/mol, which do not perturb the para-oriented arrangement of the two fluorine atoms in FSI^-. However, under stronger Li^+–anion–solvent interactions, this para-arrangement is altered in the most stable cluster configurations. And in the condensed phase, both structural isomers coexist. Decomposition of the interaction energies into electrostatic (Elst.), induction (Ind.), and dispersion (Disp.) terms reveals that, unlike BA, where dispersion and electrostatic effects are comparable, the interactions in EC, AN, and FEC are predominantly governed by electrostatic term (Figure 2b). Furthermore, polarization effects remain minimal across all systems.

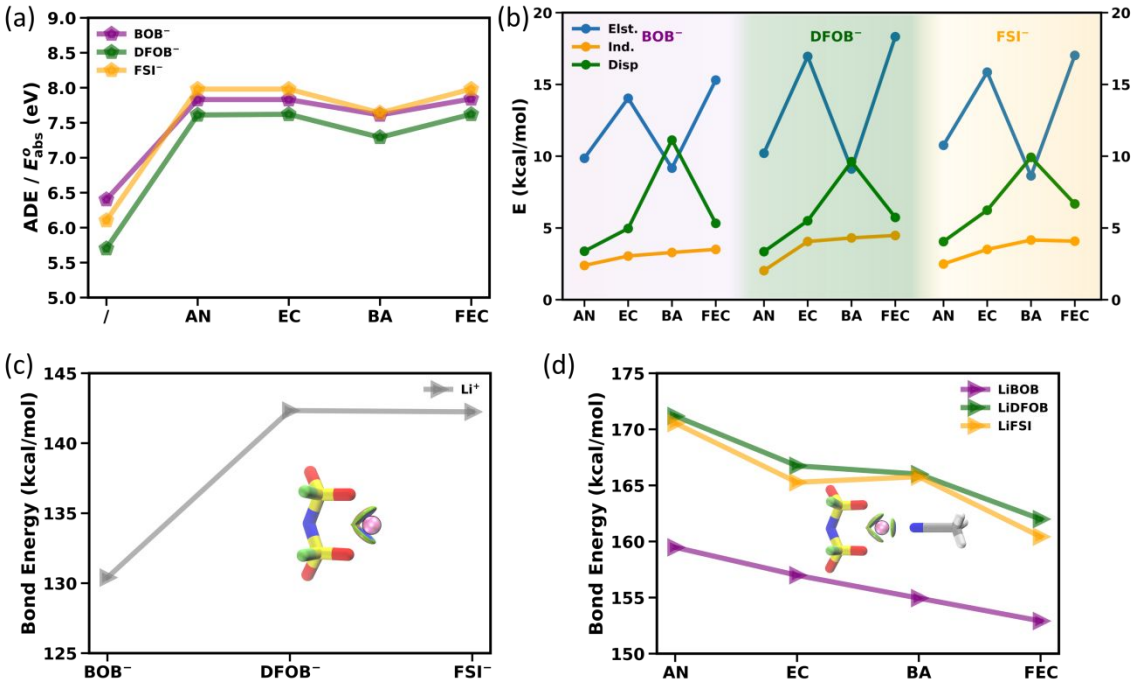

Figure 2. (a) Measured ADEs of isolated BOB^-, $DFOB^-$, FSI^-, and their corresponding absolute solution phase redox potentials (E^o_{abs}) (eV) in different solvents (solvent = AN, EC, BA and FEC). (b) Electrostatic (Elst., blue), induction (Ind., orange), and dispersion (Disp., green) attraction terms (kcal/mol) derived from energy decomposition analysis for the studied twelve anion–solvent systems. For ease of comparison, attractive terms are denoted as positive values. Lithium bond energies between Li^+ and anions (kcal/mol) (c), and between Li^+ and the combined 1:1 anion–solvent cluster (d), calculated using the SAPT2+/aug-cc-pVDZ method. Independent gradient model plots based on Hirshfeld (IGMH) partition for four types of interaction mode were inserted using FSI^- and AN as illustrative diagram, and additional diagrams are provided in Figure S4. The Li atom was colored in mauve. The data and lines are color coded based on the anion type (BOB^- in purple, $DFOB^-$ in green, and FSI^- in yellow), and used consistently throughout this work.

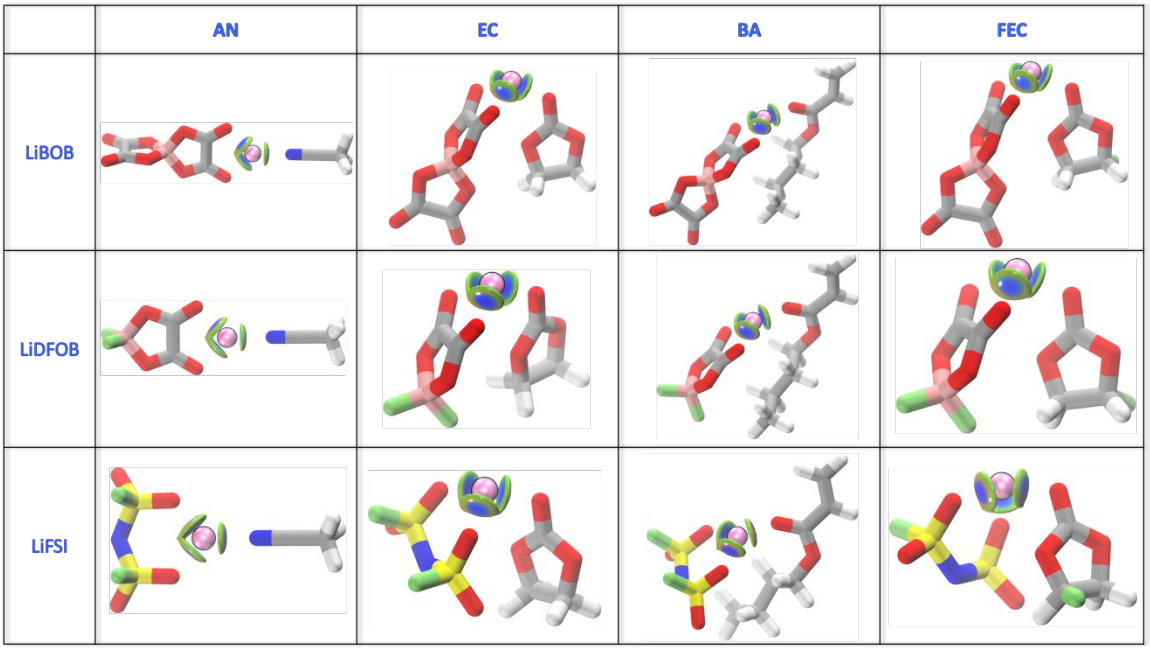

Figure 3. Independent gradient model plots based on Hirshfeld partition (IGMH) of lowest-lying energy structures for Li–anion–solvent systems (anion = BOB^-, $DFOB^-$ and FSI^-; solvent = AN, EC, BA, and FEC). Blue, green, and red color for isosurface represent the strong electrostatic interaction, the weak van der Waals interaction, and the strong repulsive interaction, respectively.

B. Binding Energy Analysis of Li^+–Anion–Solvent Interactions. To elucidate the molecular-level origins of anionic-dependent ion diffusion and coordination behavior, we employed a custom conformational search algorithm to identify three prototypical Li bond motifs in gas-phase isolated cluster mode: (1) Li^+–anion, (2) Li^+–solvent, and (3) Li^+–anion–solvent (Figure S3). The independent gradient model (IGMH) based on Hirshfeld partitioning (Figure S4) visually mapped non-covalent interactions, revealing distinct bonding characteristics across motifs. Figure 3 presents the lowest-lying energy structures of the studied Li^+–anion–solvent clusters, in which the Li^+ ion adopts a tripod-like coordination geometry involving the two donor atoms from anion and one from a solvent molecule across all twelve electrolyte systems. Each anion contributes two coordinating atoms to bind the Li^+ ion. However, in the following condensed-phase

simulations, due to the collaborative competition mode among diverse non-covalent interaction, only in the LiFSI-BA electrolyte system present double oxygen atoms coordination, similar to this idealized anion coordination motif of gas-phase cluster mode with lowest-lying energy structures.

Total Li bond energies and decomposed energy terms are presented in Figure 2c, d and S3, with the LiFSI-AN cluster serving as a representative example for Li bond interaction analysis. The Li^+ desolvation processes at electrode/electrolyte interfaces are critically governed by Li^+–solvent binding energies, which directly influence ion diffusion kinetics.[84] Our analysis of ternary Li^+–anion–solvent (1:1:1) clusters reveals that $DFOB^-$ and FSI^- exhibit Li bond energies ~10 kcal/mol higher than BOB^- (Figure 2d), independent of gas-phase Li^+–solvent interactions (Figure S4 and Table S8). This trend correlates with the intrinsic stability of Li^+–anion interactions in isolated systems (Figure 2c), underscoring the dominance of anion-mediated lithium bond in solvation complex formation. Energy decomposition analysis further highlights that Li^+–anion–solvent interactions are electrostatic-dominated, with minor induction contributions and negligible dispersion effects (Figure S5c). This interaction profile mirrors Li^+–anion binding characteristics (Figure S4a), reinforcing the central role of anion chemistry in modulating solvation dynamics. Establishing molecular-level representative stable cluster configurations in electrolyte systems helps understand the strength and nature of anion-mediated lithium bonding interactions. This provides a theoretical basis for rational anion design to balance Li^+ coordination stability and transport efficiency in advanced battery systems.

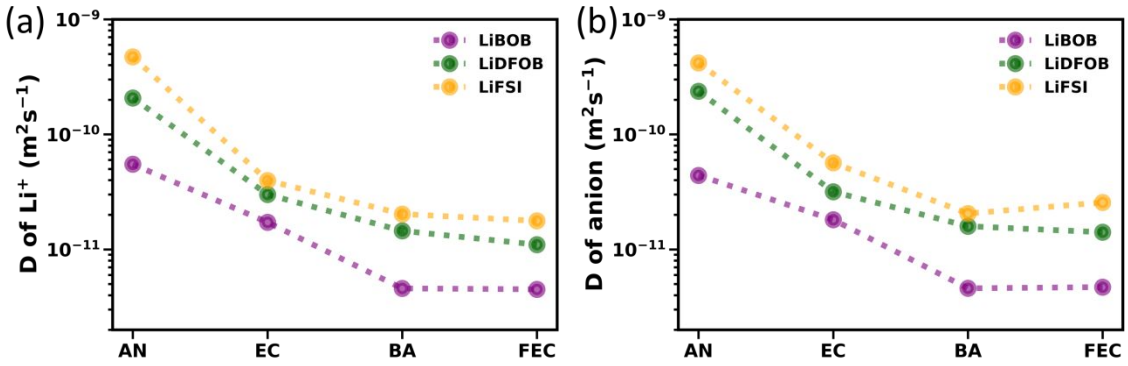

Figure 4. Self-diffusion coefficients of Li^+ (a) and anions (b) computed from MD simulations at 298.15 K for twelve Li–anion–solvent condensed systems (anion = BOB^-, $DFOB^-$, FSI^-; solvent = AN, EC, BA, FEC).

C. Anion-dominated Diffusion Coefficients. Based on the above in-depth exploration of the electronic structure of anions, twelve Li–anion–solvent electrolytes systems were selected to investigate how anion identity governs Li^+ diffusion behavior. These systems comprise 1.0 mol l^{-1} lithium salts of LiBOB, LiDFOB, or LiFSI in AN, EC, BA, or FEC solvent, respectively. The diffusion coefficients (D) of Li^+ and each anion were derived by fitting the mean-square displacements (MSD) from a 10 ns trajectory extracted from 60 ns MD simulations at 298.15 K, using Stokes−Einstein relation in equation (2).

$$D = \frac{1}{6}\frac{d\big(MSD(t)\big)}{dt} \quad (2)$$

As shown in Figure 4, the Li^+ and anion diffusion coefficients in LiDFOB and LiFSI systems exceed those in LiBOB-based electrolytes by threefold and fivefold on average, respectively, across all four solvents. This disparity underscores the critical role of anion chemistry in modulating Li^+ ion mobility. The choice of solvent also substantially impacts the underlying Li^+ diffusion mechanisms. Among the four solvents studied, AN exhibited the highest self-diffusion coefficients for both Li^+ and the anions across all lithium salts with a highest Li^+ diffusion coefficient of 4.7×10^{-10} m^2 s^{-1} achieved for LiFSI in AN among the twelve electrolyte systems. Notably, in nitrogen-containing

electrolytes, the Li^+ diffusion coefficient slightly surpasses the corresponding anion, i.e., 4.7 vs. 4.2 × 10^{-10} m^2 s^{-1} in LiFSI-AN, and 0.6 vs. 0.4 × 10^{-10} m^2 s^{-1} in LiBOB-AN (Table S9). This decoupling of Li^+ and anion transport activity suggests that ionic diffusion is no longer limited by the salt anion in such systems. These results align with previous studies demonstrating enhanced Li^+ diffusion in nitrogen-containing solvents.[38, 85-86] In EC, the Li^+ diffusion coefficients in LiDFOB and LiFSI are comparable, both outperforming BOB^-. Notably, EC exhibits the smallest disparity in Li^+ diffusion efficient between LiFSI/LiDFOB and LiBOB, highlighting its broad compatibility with diverse lithium salts. For BA and FEC, solvent substitution has minimal impact on Li^+ and anion diffusion coefficients within the same lithium salt. LiFSI and LiDFOB systems also maintain higher ionic diffusivities than LiBOB in BA and FEC, consistent with the trends in AN and EC. These findings demonstrate that FSI^- and $DFOB^-$ anions are promising candidates for next-generation electrolyte formulations. And AN solvent containing a −CN group can be considered as an efficient additive solvent to promote ion diffusion.

D. Solvation structure of Li^+. Characterizing the anion-mediated Li^+ coordination shell is essential for understanding Li^+ diffusion mechanisms in electrolyte systems. The radial distribution functions (RDFs) and cumulative coordination numbers (CNs) were analyzed for oxygen atoms at the terminal ends of anions/solvents and fluorine atoms in $DFOB^-$/FSI^- coordinating with Li^+ (Figure S6). Across all 12 electrolytes, the total Li^+ coordination number approaches 5, except for LiDFOB-AN (4.52), as shown in Figure 5 and Table S10. The electronic structural properties and charge distribution of the anions determine the specific sites through which each anion participates in Li^+ coordination. In the LiBOB series, the four oxygen atoms at BOB^- termini predominantly coordinate with Li^+. For $DFOB^-$, both oxygen and fluorine atoms participate in coordination. In contrast, only the oxygen atoms of FSI^- contribute to the primary Li^+ coordination shell, while fluorine atoms are excluded across all solvents. In contrast to the well-defined tripod

geometry of Li^+ coordination in the gas-phase cluster model, only one oxygen atom per anion coordinates with Li^+ in BOB^- and $DFOB^-$ electrolyte systems, with negligible simultaneous coordination of two oxygen atoms (< 0.01%). Conversely, FSI^- allows two oxygen atoms from a single anion to coordinate with Li^+ simultaneously as shown in LiFSI-BA electrolyte.

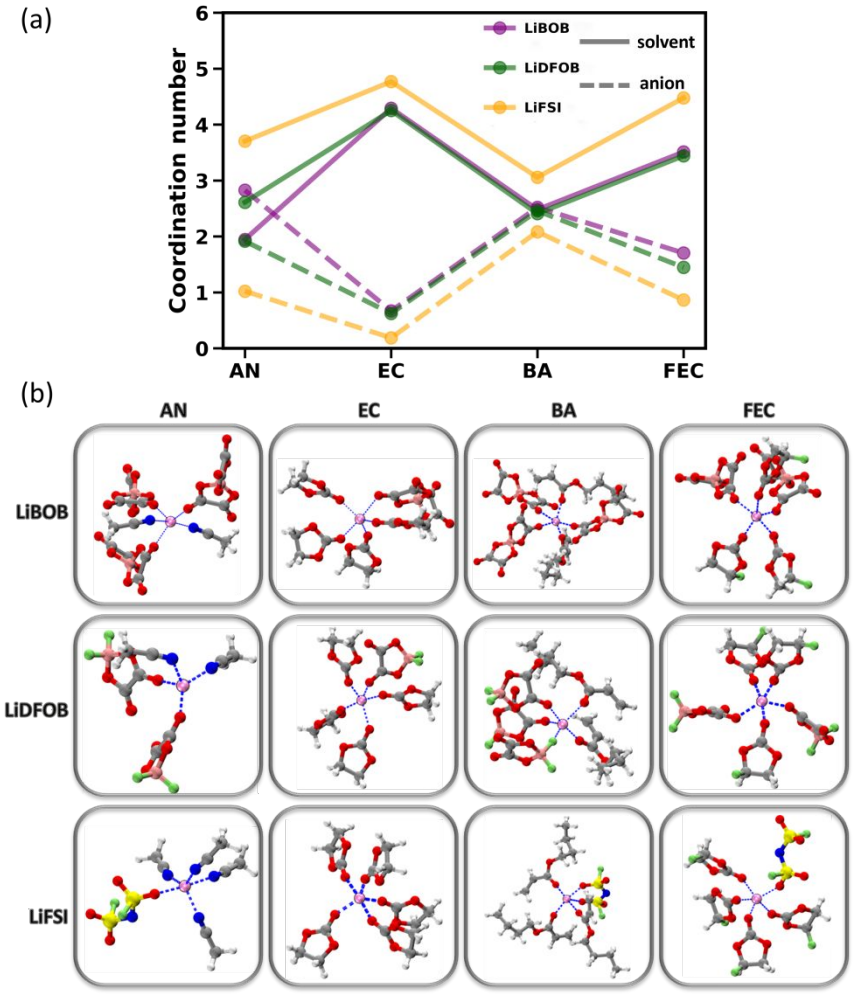

Figure 5. (a) Li^+ coordination number (CN) contributed from solvent (solid line) and anion (dashed line) with a threshold distance cut of 2.4 Å in LiBOB (purple), LiDFOB (green) and LiFSI (orange) in combination with four solvents derived from running integrals in MD simulations. The CN of anion is denoted as the summations of O and F atoms coordinating to Li^+, except for LiFSI-BA. The Li^+ CN from O atoms in isolated

LiFSI⁻ salt is 2, while it should be considered as 1.4 FSI^- coordinated to Li^+ (1×0.6 + 2×0.4), as the FSI^- in BA adopts dual oxygen coordination from 1 or 2 anions, yielding a mixed CIP/AGG solvating population (60% CIP, 40% AGG). (b) Representative snapshots from MD simulations depicting the first compact coordination shell within 2.4 Å of Li^+ cations in simulation cubic box.

As shown in Figure 5a and listed in Table S10, EC predominantly occupies the first solvation shell, with minimal anion participation. In LiFSI-EC, FSI^- rarely forms contact ion pairs (CIP), resembling the behavior of $LiPF_6$-EC.[87] Conversely, LiBOB-EC and LiDFOB-EC primarily form contact ion pairs (CIP). This inclusion of anions in the coordination shell—without compromising Li^+ diffusivity—can enhance anion reduction on the anode, producing inorganic components to promote rigidity solid-electrolyte interphase (SEI) formation.[27-28] As for AN solvent, it reduces solvent coordination while increasing anion participation for three salts. LiBOB-AN and LiDFOB-AN predominantly form aggregated (AGG) solvates (Figure 5b), where two oxygen atoms from separate anions coordinate with Li^+. This nitrile-based solvent's ability to promote anion participation may improve long-term cycling stability.[88] The LiFSI-BA system displays an average FSI^- coordination number of 1.4, arising from two scenarios: (i) bidentate coordination by a single FSI^- anion through its two oxygen atoms forming CIP (60% prevalence), (ii) bridging coordination involving two separate FSI^- anions forming AGG solvates (40% prevalence). Beyond EC, the addition of AN, BA, or FEC enhances anion participation in the Li^+ solvation shell, thereby optimizing SEI formation in varying degrees.[88]

Ⅳ. CONCLUSIONS

This study presents a molecular-level investigation into the interplay between anion chemistry, solvation structure, and Li^+ transport behavior in advanced lithium battery electrolytes. By integrating cryogenic NIPES, *ab initio* calculations, and MD simulations,

we establish a multi-scale framework for understanding how intrinsic electronic structural properties of anions—specifically $DFOB^-$, FSI^-, and BOB^-—govern their interactions with solvation structure and ion transport behavior. NIPES measurements reveal that all three anions exhibit high electron binding energies, with vertical and adiabatic detachment energies increasing from $DFOB^-$ (6.09/5.70 eV) to FSI^- (6.80/6.10 eV), and further to BOB^- (6.82/6.40 eV). This trend correlates well with enhanced oxidative stability and highlights the importance of electronic structure in determining anion performance and is closely tied to the spatial distribution of HOMO. Notably, FSI^- exists as two low-lying energy isomers—FSI^-_{contra} and FSI^-_{ipsi}—with minimal energy difference (1.11 kcal/mol) and similar charge localization, where electron removal predominantly involves O and N atoms rather than F atoms. In contrast, $DFOB^-$ shows pronounced negative charge localization on its terminal fluorine and oxygen atoms, enabling both participation primary Li^+ coordination shell, particularly in the LiDFOB–BA system. While, the less electron-rich fluorine atoms in FSI^- series are excluded from Li^+ coordination across all solvents. These findings highlight the critical role of anion-specific electronic structures in shaping local solvation environments.

Based on the most stable Li^+–anion–solvent cluster constructed by our self-made searching strategy, *ab initio* calculations reveal that $DFOB^-$ and FSI^- form significantly stronger Li bond interactions (~10 kcal/mol higher than BOB^- series), primarily due to electrostatic dominance over induction and dispersion effects. Under the cooperative competition mode of dynamic non-covalent interaction, only in LiFSI-BA electrolyte, FSI^- uniquely allow dual-oxygen atoms coordinating to Li^+ via two S-N bonds of a single anion, resembling the ideal tripod-type Li^+ coordination motif in Li^+–anion–solvent gas phase clusters. MD simulations further demonstrate that the identity of the anion has a profound influence on Li^+ diffusion kinetics. On average, LiDFOB and LiFSI series electrolytes exhibit Li^+ diffusion coefficients three and five times higher than those of LiBOB, respectively, across four representative solvents. Among these, AN emerges as

the most effective solvent, with the LiFSI-AN system achieving a Li^+ diffusion coefficient of 4.7×10^{-10} m^2 s^{-1}, ten times than that of the conventional LiFSI-EC electrolytes.

These findings provide the rational design of high-performance electrolytes by linking fundamental anion properties—including electronic structure, charge distribution, and solvation effect—with macroscopic transport and interfacial phenomena. Our results highlight the promise of FSI^- and $DFOB^-$ as leading candidates for next-generation lithium battery systems, especially when combined with functional solvents like acetonitrile that enhance both solvation and ion mobility. Future work will employ deep potential−range correction machine learning potential[89] methods to quantify desolvation free energies to bridge the anion-specific solvation dynamics and interfacial kinetics in advanced battery systems.

ASSOCIATED CONTENTS

Supporting Information

Computational Details: Calculated VDE using various methods with the aug-cc-pVTZ basis set; detailed configuration search methodology for Li^+-anion-solvent cluster; fitting restrained electrostatic potential ($RESP2_{0.5}$) charges; simulation cell lengths (Å) and number of molecules for MD simulations; calculated VDEs for mono-solvated clusters; energy decomposition analysis based on SAPT2+/aug-cc-pVDZ method; RDF and the corresponding cumulative number; the lowest-lying energy structures for Li^+–anion, Li^+–solvent, anion–solvent, and Li–anion–solvent systems and corresponding IGMH plots; electrostatic potential (ESP) maps;

geometric structures for anions and corresponding clusters.

AUTHOR DECLEARTIONS

Corresponding Author

Xue-Bin Wang − Physical Sciences Division, Pacific Northwest National Laboratory, Washington 99352, USA; orcid.org/0000-0001-8326-1780; Email:xuebin.wang@pnnl.gov.

Zhubin Hu − State Key Laboratory of Precision Spectroscopy, East China Normal University, Shanghai 200241, China; Email: zbhu@lps.ecnu.edu.cn.

Weijia Zhang − School of Mathematics Information, Shaoxing University, Zhejiang 312000, China; Email: zhangusx@yeah.net.

Authors

Yanrong Jiang − School of Mathematics Information, Shaoxing University, Zhejiang 312000, China; orcid.org/0000-0002-1508-6770

Wenjin Cao − Physical Sciences Division, Pacific Northwest National Laboratory, Washington 99352, USA

Xiao-Fei Gao − Physical Sciences Division, Pacific Northwest National Laboratory, Washington 99352, USA

Jinzhe Zeng − School of Artificial Intelligence and Data Science, University of Science and Technology of China, Hefei 230026, China; Suzhou Institute for Advanced Research, University of Science and Technology of China, Suzhou 215123, China; Suzhou Big Data & AI Research and Engineering Center, Suzhou 215123, China

Haoyu Cao − School of Mathematics Information, Shaoxing University, Zhejiang 312000, China

Shunwei Zhu − School of Mathematics Information, Shaoxing University, Zhejiang 312000, China

Wenhao Wang − School of Mathematics Information, Shaoxing University, Zhejiang 312000, China

Xue Cheng − School of Mathematics Information, Shaoxing University, Zhejiang 312000, China

Dongqin Sun − School of Mathematics Information, Shaoxing University, Zhejiang 312000, China

Feiyu Chen − School of Mathematics Information, Shaoxing University, Zhejiang 312000, China

Notes

The authors declare no competing financial interest.

ACKNOWLEDGEMENTS

This work is supported by the National Natural Science Foundation of China (12304284, 12204172). The NIPES work was supported by the U.S. Department of Energy (DOE), Office of Science, Office of Basic Energy Sciences, Division of Chemical Sciences, Geosciences, and Biosciences, Condensed Phase and Interfacial Molecular Science program (No. FWP 16248). This research was also supported by the advanced computing resources provided by the Supercomputing Center of University of science and Technology of China.

REFERENCES

(1) Li, M.; Lu, J.; Chen, Z.; Amine, K. 30 Years of Lithium-Ion Batteries. *Adv. Mater.* **2018**, *30*, 1800561.

(2) Jia, R.; Dai, H.; Tu, X.; Sun, C.; Sun, S.; Lai, C. Hexabutylcyclohexane-1,2,3,4,5,6-hexaimine Additive-Assisted Commercial Ester Electrolyte for 4.7 V Highly-Stable Li-Metal Batteries. *Adv. Energy Mater.* **2023**, *13*, 2302747.

(3) Zhu, X.; Huang, A.; Martens, I.; Vostrov, N.; Sun, Y.; Richard, M.-I.; Schülli, T. U.; Wang, L. High-Voltage Spinel Cathode Materials: Navigating the Structural Evolution for Lithium-Ion Batteries. *Adv. Mater.* **2024**, *36*, 2403482.

(4) Hahn, N. T.; Seguin, T. J.; Lau, K.-C.; Liao, C.; Ingram, B. J.; Persson, K. A.; Zavadil, K. R. Enhanced Stability of the Carba-closo-dodecaborate Anion for High-Voltage Battery Electrolytes through Rational Design. *J. Am. Chem. Soc.* **2018**, *140*, 11076-11084.

(5) Dou, F.; Shi, L.; Chen, G.; Zhang, D. Silicon/Carbon Composite Anode Materials for Lithium-Ion Batteries. *Electrochem. Energy Rev.* **2019**, *2*, 149-198.

(6) Zhang, X.; Wang, D.; Qiu, X.; Ma, Y.; Kong, D.; Müllen, K.; Li, X.; Zhi, L. Stable high-capacity and high-rate silicon-based lithium battery anodes upon two-dimensional covalent encapsulation. *Nat. Commun.* **2020**, *11*, 3826.

(7) Kim, S. C.; Oyakhire, S. T.; Athanitis, C.; Wang, J.; Zhang, Z.; Zhang, W.; Boyle, D. T.; Kim, M. S.; Yu, Z.; Gao, X.; et al. Data-driven electrolyte design for lithium metal anodes. *Proc. Natl. Acad. Sci.* **2023**, *120*, e2214357120.

(8) Lu, G.; Nai, J.; Luan, D.; Tao, X.; Lou, X. W. Surface engineering toward stable lithium metal anodes. *Sci. Adv.*, *9*, eadf1550.

(9) Li, A.-M.; Borodin, O.; Pollard, T. P.; Zhang, W.; Zhang, N.; Tan, S.; Chen, F.; Jayawardana, C.; Lucht, B. L.; Hu, E.; et al. Methylation enables the use of fluorine-free ether electrolytes in high-voltage lithium metal batteries. *Nat. Chem.* **2024**, *16*, 922-929.

(10) He, X.; Bresser, D.; Passerini, S.; Baakes, F.; Krewer, U.; Lopez, J.; Mallia, C. T.; Shao-Horn, Y.; Cekic-Laskovic, I.; Wiemers-Meyer, S.; et al. The passivity of lithium electrodes in liquid electrolytes for secondary batteries. *Nat. Rev. Mater.* **2021**, *6*, 1036-1052.

(11) Cheng, X.-B.; Yan, C.; Zhang, X.-Q.; Liu, H.; Zhang, Q. Electronic and Ionic Channels in Working Interfaces of Lithium Metal Anodes. *ACS Energy Lett.* **2018**, *3*, 1564-1570.

(12) Xu, J.; Zhang, J.; Pollard, T. P.; Li, Q.; Tan, S.; Hou, S.; Wan, H.; Chen, F.; He, H.; Hu, E.; et al. Electrolyte design for Li-ion batteries under extreme operating conditions. *Nature* **2023**, *614*, 694-700.

(13) Xu, K. Nonaqueous Liquid Electrolytes for Lithium-Based Rechargeable Batteries.

Chem. Rev. **2004**, *104*, 4303-4418.
(14) Wang, Z.; Zhang, B. Weakly solvating electrolytes for next-generation lithium batteries: design principles and recent advances. *Energy Mater. Devices* **2023**, *1*, 9370003.
(15) Xu, K. Electrolytes and Interphases in Li-Ion Batteries and Beyond. *Chem. Rev.* **2014**, *114*, 11503-11618.
(16) Huang, Z.; Li, X.; Chen, Z.; Li, P.; Ji, X.; Zhi, C. Anion chemistry in energy storage devices. *Nat. Rev. Chem.* **2023**, *7*, 616-631.
(17) Xiao, H.; Li, X.; Fu, Y. Advances in Anion Chemistry in the Electrolyte Design for Better Lithium Batteries. *Nano-Micro Lett.* **2025**, *17*, 149.
(18) Chai, D.; Yan, H.; Wang, X.; Li, X.; Fu, Y. Retuning Solvating Ability of Ether Solvent by Anion Chemistry toward 4.5 V Class Li Metal Battery. *Adv. Funct. Mater.* **2024**, *34*, 2310516.
(19) Yuan, S.; Cao, S.; Chen, X.; Wei, J.; Lv, Z.; Xia, H.; Li, J.; Zhang, H.; Liu, L.; Tian, C.; et al. Deshielding Anions Enable Solvation Chemistry Control of LiPF6-Based Electrolyte toward Low-Temperature Lithium-Ion Batteries. *Adv. Mater.* **2024**, *36*, 2311327.
(20) Wang, Z.; Qi, F.; Yin, L.; Shi, Y.; Sun, C.; An, B.; Cheng, H.-M.; Li, F. Lithium Anodes: An Anion-Tuned Solid Electrolyte Interphase with Fast Ion Transfer Kinetics for Stable Lithium Anodes. *Adv. Energy Mater.* **2020**, *10*, 2070063.
(21) Zhu, X.; Chen, J.; Liu, G.; Mo, Y.; Xie, Y.; Zhou, K.; Wang, Y.; Dong, X. Non-Fluorinated Cyclic Ether-Based Electrolyte with Quasi-Conjugate Effect for High-Performance Lithium Metal Batteries. *Angew. Chem. Int. Ed.* **2025**, *64*, e202412859.
(22) Zhang, W.; Zhuang, H. L.; Fan, L.; Gao, L.; Lu, Y. A "cation-anion regulation" synergistic anode host for dendrite-free lithium metal batteries. *Sci. Adv.*, *4*, eaar4410.
(23) Chen, L.; Lu, J.; Wang, Y.; He, P.; Huang, S.; Liu, Y.; Wu, Y.; Cao, G.; Wang, L.; He, X.; et al. Double-salt electrolyte for Li-ion batteries operated at elevated temperatures. *Energy Storage Mater.* **2022**, *49*, 493-501.
(24) Ding, F.; Xu, W.; Chen, X.; Zhang, J.; Engelhard, M. H.; Zhang, Y.; Johnson, B. R.; Crum, J. V.; Blake, T. A.; Liu, X.; et al. Effects of Carbonate Solvents and Lithium Salts on Morphology and Coulombic Efficiency of Lithium Electrode. *J. Electrochem. Soc.* **2013**, *160*, A1894.
(25) Zhao, Y.; Zhou, T.; Ashirov, T.; Kazzi, M. E.; Cancellieri, C.; Jeurgens, L. P. H.; Choi, J. W.; Coskun, A. Fluorinated ether electrolyte with controlled solvation structure for high voltage lithium metal batteries. *Nat. Commun.* **2022**, *13*, 2575.
(26) Xu, J.; Koverga, V.; Phan, A.; min Li, A.; Zhang, N.; Baek, M.; Jayawardana, C.; Lucht, B. L.; Ngo, A. T.; Wang, C. Revealing the Anion–Solvent Interaction for Ultralow Temperature Lithium Metal Batteries. *Adv. Mater.* **2024**, *36*, 2306462.
(27) Yu, W.; Lin, K.-Y.; Boyle, D. T.; Tang, M. T.; Cui, Y.; Chen, Y.; Yu, Z.; Xu, R.; Lin, Y.; Feng, G.; et al. Electrochemical formation of bis(fluorosulfonyl)imide-derived solid-electrolyte interphase at Li-metal potential. *Nat. Chem.* **2025**, *17*, 246-255.

(28) Wang, H.; Huang, W.; Yu, Z.; Huang, W.; Xu, R.; Zhang, Z.; Bao, Z.; Cui, Y. Efficient Lithium Metal Cycling over a Wide Range of Pressures from an Anion-Derived Solid-Electrolyte Interphase Framework. *ACS Energy Lett.* **2021**, *6*, 816-825.
(29) Ko, S.; Han, X.; Shimada, T.; Takenaka, N.; Yamada, Y.; Yamada, A. Electrolyte design for lithium-ion batteries with a cobalt-free cathode and silicon oxide anode. *Nat. Sustain.* **2023**, *6*, 1705-1714.
(30) Fawdon, J.; Ihli, J.; Mantia, F. L.; Pasta, M. Characterising lithium-ion electrolytes via operando Raman microspectroscopy. *Nat. Commun.* **2021**, *12*, 4053.
(31) Song, Z.; Wang, X.; Wu, H.; Feng, W.; Nie, J.; Yu, H.; Huang, X.; Armand, M.; Zhang, H.; Zhou, Z. Bis(fluorosulfonyl)imide-based electrolyte for rechargeable lithium batteries: A perspective. *J. Power Sources Adv.* **2022**, *14*, 100088.
(32) Melin, T.; Lundström, R.; Berg, E. J. Elucidating the Reduction Mechanism of Lithium Bis(oxalato)borate. *J. Phys. Chem. Lett.* **2024**, *15*, 2537-2541.
(33) Xiao, Y.; Wang, X.; Yang, K.; Wu, J.; Chao, Y.; Xi, C.; Li, M.; Zhang, Q.; Liu, Z.; Li, L.; et al. The Anion-Dominated Dynamic Coordination Field in the Electrolytes for High-Performance Lithium Metal Batteries. *Energy Storage Mater.* **2023**, *55*, 773-781.
(34) Yao, N.; Chen, X.; Sun, S.-Y.; Gao, Y.-C.; Yu, L.; Gao, Y.-B.; Li, W.-L.; Zhang, Q. Identifying the lithium bond and lithium ionic bond in electrolytes. *Chem* **2025**, *11*, 102254.
(35) Chen, X.; Bai, Y.-K.; Zhao, C.-Z.; Shen, X.; Zhang, Q. Lithium Bonds in Lithium Batteries. *Angew. Chem. Int. Ed.* **2020**, *59*, 11192-11195.
(36) Hou, T.-Z.; Xu, W.-T.; Chen, X.; Peng, H.-J.; Huang, J.-Q.; Zhang, Q. Lithium Bond Chemistry in Lithium–Sulfur Batteries. *Angew. Chem. Int. Ed.* **2017**, *56*, 8178-8182.
(37) Park, K.; Cho, J. H.; Jang, J.-H.; Yu, B.-C.; De La Hoz, A. T.; Miller, K. M.; Ellison, C. J.; Goodenough, J. B. Trapping lithium polysulfides of a Li–S battery by forming lithium bonds in a polymer matrix. *Energy Environ. Sci.* **2015**, *8*, 2389-2395.
(38) Yamada, Y.; Furukawa, K.; Sodeyama, K.; Kikuchi, K.; Yaegashi, M.; Tateyama, Y.; Yamada, A. Unusual Stability of Acetonitrile-Based Superconcentrated Electrolytes for Fast-Charging Lithium-Ion Batteries. *J. Am. Chem. Soc.* **2014**, *136*, 5039-5046.
(39) Zhu, C.; Lv, W.; Chen, J.; Ou, C.; Zhang, Q.; Fu, H.; Wang, H.; Wu, L.; Zhong, S. Butyl acrylate (BA) and ethylene carbonate (EC) electrolyte additives for low-temperature performance of lithium ion batteries. *J. Power Sources* **2020**, *476*, 228697.
(40) Yuan, Q.; Wenjin, C.; and Wang, X.-B. Cryogenic and temperature-dependent photoelectron spectroscopy of metal complexes. *Int. Rev. Phys. Chem.* **2020**, *39*, 83-108.
(41) Wang, X.-B.; Wang, Y.-L.; Yang, J.; Xing, X.-P.; Li, J.; Wang, L.-S. Evidence of Significant Covalent Bonding in $Au(CN)^{2-}$. *J. Am. Chem. Soc.* **2009**, *131*, 16368-16370.
(42) Hanstorp, D.; Gustafsson, M. Determination of the electron affinity of iodine. *J. Phys. B:At., Mol. Opt. Phys.* **1992**, *25*, 1773.
(43) Jiang, Y.; Cai, Z.; Yuan, Q.; Cao, W.; Hu, Z.; Sun, H.; Wang, X.-B.; Sun, Z. Highly Structured Water Networks in Microhydrated Dodecaborate Clusters. *J. Phys. Chem. Lett.* **2022**, *13*, 11787-11794.

(44) Jiang, Y.; Yuan, Q.; Cao, W.; Hu, Z.; Yang, Y.; Zhong, C.; Yang, T.; Sun, H.; Wang, X.-B.; Sun, Z. Unraveling hydridic-to-protonic dihydrogen bond predominance in monohydrated dodecaborate clusters. *Chem. Sci.* **2022**, *13*, 9855-9860.
(45) Lu, T. *Molclus Program*, Beijing Kein Research Center for Natural Science: 2016.
(46) Bannwarth, C.; Ehlert, S.; Grimme, S. GFN2-xTB—An Accurate and Broadly Parametrized Self-Consistent Tight-Binding Quantum Chemical Method with Multipole Electrostatics and Density-Dependent Dispersion Contributions. *J. Chem. Theory Comput.* **2019**, *15*, 1652-1671.
(47) Bursch, M.; Neugebauer, H.; Grimme, S. Structure Optimisation of Large Transition-Metal Complexes with Extended Tight-Binding Methods. *Angew. Chem. Int. Ed.* **2019**, *58*, 11078-11087.
(48) Neese, F. Software update: The ORCA program system—Version 5.0. *WIREs Comput. Mol. Sci.* **2022**, *12*, e1606.
(49) Chai, J.-D.; Head-Gordon, M. Long-range corrected double-hybrid density functionals. *J. Chem. Phys.* **2009**, *131*, 174105.
(50) Chai, J.-D.; Head-Gordon, M. Long-range corrected hybrid density functionals with damped atom–atom dispersion corrections. *Phys. Chem. Chem. Phys.* **2008**, *10*, 6615-6620.
(51) Kendall, R. A.; Dunning, T. H., Jr.; Harrison, R. J. Electron affinities of the first-row atoms revisited. Systematic basis sets and wave functions. *J. Chem. Phys.* **1992**, *96*, 6796-6806.
(52) Grimme, S.; Antony, J.; Ehrlich, S.; Krieg, H. A Consistent and Accurate ab initio Parametrization of Density Functional Dispersion Correction (DFT-D) for the 94 Elements H-Pu. *J. Chem. Phys.* **2010**, *132*, 154104.
(53) Grimme, S.; Ehrlich, S.; Goerigk, L. Effect of the Damping Function in Dispersion Corrected Density Functional Theory. *J. Comput. Chem.* **2011**, *32*, 1456-1465.
(54) Riplinger, C.; Sandhoefer, B.; Hansen, A.; Neese, F. Natural Triple Excitations in Local Coupled Cluster Calculations with Pair Natural Orbitals. *J. Chem. Phys.* **2013**, *139*, 134101.
(55) Neese, F.; Wennmohs, F.; Hansen, A. Efficient and Accurate Local Approximations to Coupled-Electron Pair Approaches: An Attempt to Revive the Pair Natural Orbital Method. *J. Chem. Phys.* **2009**, *130*, 114108.
(56) Merrick, J. P.; Moran, D.; Radom, L. An Evaluation of Harmonic Vibrational Frequency Scale Factors. *J. Phys. Chem. A* **2007**, *111*, 11683-700.
(57) Adamo, C.; Barone, V. Toward reliable density functional methods without adjustable parameters: The PBE0 model. *J. Chem. Phys.* **1999**, *110*, 6158-6170.
(58) Stephens, P. J.; Devlin, F. J.; Chabalowski, C. F.; Frisch, M. J. Ab initio calculation of vibrational absorption and circular dichroism spectra using density functional force fields. *J. Phys. Chem.* **1994**, *98*, 11623-11627.
(59) Zhao, Y.; Truhlar, D. G. The M06 suite of density functionals for main group thermochemistry, thermochemical kinetics, noncovalent interactions, excited states, and

transition elements: two new functionals and systematic testing of four M06-class functionals and 12 other functionals. *Theor. Chem. Acc.* **2008**, *120*, 215-241.
(60) Dutta, A. K.; Saitow, M.; Riplinger, C.; Neese, F.; Izsák, R. A near-linear scaling equation of motion coupled cluster method for ionized states. *J. Chem. Phys.* **2018**, *148*, 244101.
(61) Hohenstein, E. G.; Sherrill, C. D. Density Fitting of Intramonomer Correlation Effects in Symmetry-Adapted Perturbation Theory. *J. Chem. Phys.* **2010**, *133*, 014101.
(62) Parker, T. M.; Burns, L. A.; Parrish, R. M.; Ryno, A. G.; Sherrill, C. D. Levels of Symmetry Adapted Perturbation Theory (SAPT). I. Efficiency and Performance for Interaction Energies. *J. Chem. Phys.* **2014**, *140*, 094106.
(63) Parrish, R. M.; Burns, L. A.; Smith, D. G. A.; Simmonett, A. C.; DePrince, A. E.; Hohenstein, E. G.; Bozkaya, U.; Sokolov, A. Y.; Di Remigio, R.; Richard, R. M.; et al. Psi4 1.1: An Open-Source Electronic Structure Program Emphasizing Automation, Advanced Libraries, and Interoperability. *J. Chem. Theory Comput.* **2017**, *13*, 3185-3197.
(64) Lu, T.; Chen, F. Multiwfn: A multifunctional wavefunction analyzer. *J. Comput. Chem.* **2012**, *33*, 580-592.
(65) Humphrey, W.; Dalke, A.; Schulten, K. VMD: Visual molecular dynamics. *J. Mol. Graph.* **1996**, *14*, 33-38.
(66) Frisch, M. J.; Trucks, G. W.; Schlegel, H. B.; Scuseria, G. E.; Robb, M. A.; Cheeseman, J. R.; Scalmani, G.; Barone, V.; Petersson, G. A.; Nakatsuji, H.; et al. *Gaussian 16 Rev. B.01*, Wallingford, CT, 2016.
(67) Abraham, M. J.; Murtola, T.; Schulz, R.; Páll, S.; Smith, J. C.; Hess, B.; Lindahl, E. GROMACS: High performance molecular simulations through multi-level parallelism from laptops to supercomputers. *SoftwareX* **2015**, *1-2*, 19-25.
(68) Wang, J.; Wolf, R. M.; Caldwell, J. W.; Kollman, P. A.; Case, D. A. Development and testing of a general amber force field. *J. Comput. Chem.* **2004**, *25*, 1157-1174.
(69) Rappe, A. K.; Casewit, C. J.; Colwell, K. S.; Goddard, W. A., III; Skiff, W. M. UFF, a full periodic table force field for molecular mechanics and molecular dynamics simulations. *J. Am. Chem. Soc.* **1992**, *114*, 10024-10035.
(70) Soetens, J.-C.; Millot, C.; Maigret, B. Molecular Dynamics Simulation of Li^+BF4^- in Ethylene Carbonate, Propylene Carbonate, and Dimethyl Carbonate Solvents. *J. Phys. Chem. A* **1998**, *102*, 1055-1061.
(71) Rajput, N. N.; Murugesan, V.; Shin, Y.; Han, K. S.; Lau, K. C.; Chen, J.; Liu, J.; Curtiss, L. A.; Mueller, K. T.; Persson, K. A. Elucidating the Solvation Structure and Dynamics of Lithium Polysulfides Resulting from Competitive Salt and Solvent Interactions. *Chem. Mater.* **2017**, *29*, 3375-3379.
(72) Takeuchi, M.; Kameda, Y.; Umebayashi, Y.; Ogawa, S.; Sonoda, T.; Ishiguro, S.-i.; Fujita, M.; Sano, M. Ion–ion interactions of $LiPF_6$ and $LiBF_4$ in propylene carbonate solutions. *J. Mol. Liq* **2009**, *148*, 99-108.
(73) Wang, Z.; Ji, H.; Zhou, J.; Zheng, Y.; Liu, J.; Qian, T.; Yan, C. Exploiting nonaqueous self-stratified electrolyte systems toward large-scale energy storage. *Nat.*

Commun. **2023**, *14*, 2267.
(74) Qin, T.; Yang, H.; Wang, L.; Xue, W.; Yao, N.; Li, Q.; Chen, X.; Yang, X.; Yu, X.; Zhang, Q.; et al. Molecule Design for Non-Aqueous Wide-Temperature Electrolytes via the Intelligentized Screening Method. *Angew. Chem. Int. Ed.* **2024**, *63*, e202408902.
(75) Ma, X.; Fu, H.; Shen, J.; Zhang, D.; Zhou, J.; Tong, C.; Rao, A. M.; Zhou, J.; Fan, L.; Lu, B. Green Ether Electrolytes for Sustainable High-voltage Potassium Ion Batteries. *Angew. Chem. Int. Ed.* **2023**, *62*, e202312973.
(76) Martínez, L.; Andrade, R.; Birgin, E. G.; Martínez, J. M. PACKMOL: A package for building initial configurations for molecular dynamics simulations. *J. Comput. Chem.* **2009**, *30*, 2157-2164.
(77) Bussi, G.; Donadio, D.; Parrinello, M. Canonical sampling through velocity rescaling. *J. Chem. Phys.* **2007**, *126*, 014101.
(78) Berendsen, H. J. C.; Postma, J. P. M.; van Gunsteren, W. F.; DiNola, A.; Haak, J. R. Molecular dynamics with coupling to an external bath. *J. Chem. Phys.* **1984**, *81*, 3684-3690.
(79) Hess, B.; Bekker, H.; Berendsen, H. J. C.; Fraaije, J. G. E. M. LINCS: A linear constraint solver for molecular simulations. *J. Comput. Chem.* **1997**, *18*, 1463-1472.
(80) Essmann, U.; Perera, L.; Berkowitz, M. L.; Darden, T.; Lee, H.; Pedersen, L. G. A smooth particle mesh Ewald method. *J. Chem. Phys.* **1995**, *103*, 8577-8593.
(81) Neuhaus, J.; Bellaire, D.; Kohns, M.; von Harbou, E.; Hasse, H. Self-Diffusion Coefficients in Solutions of Lithium Bis(fluorosulfonyl)imide with Dimethyl Carbonate and Ethylene Carbonate. *Chem. Ing. Tech.* **2019**, *91*, 1633-1639.
(82) Marenich, A. V.; Cramer, C. J.; Truhlar, D. G. Universal Solvation Model Based on Solute Electron Density and on a Continuum Model of the Solvent Defined by the Bulk Dielectric Constant and Atomic Surface Tensions. *J. Phys. Chem. B* **2009**, *113*, 6378-6396.
(83) Borodin, O.; Behl, W.; Jow, T. R. Oxidative Stability and Initial Decomposition Reactions of Carbonate, Sulfone, and Alkyl Phosphate-Based Electrolytes. *J. Phys. Chem. C* **2013**, *117*, 8661-8682.
(84) Holoubek, J.; Liu, H.; Wu, Z.; Yin, Y.; Xing, X.; Cai, G.; Yu, S.; Zhou, H.; Pascal, T. A.; Chen, Z.; et al. Tailoring electrolyte solvation for Li metal batteries cycled at ultra-low temperature. *Nat. Energy* **2021**, *6*, 303-313.
(85) Peng, Z.; Freunberger, S. A.; Hardwick, L. J.; Chen, Y.; Giordani, V.; Bardé, F.; Novák, P.; Graham, D.; Tarascon, J.-M.; Bruce, P. G. Oxygen Reactions in a Non-Aqueous Li^+ Electrolyte. *Angew. Chem. Int. Ed.* **2011**, *50*, 6351-6355.
(86) Li, Z.; Borodin, O.; Smith, G. D.; Bedrov, D. Effect of Organic Solvents on Li^+ Ion Solvation and Transport in Ionic Liquid Electrolytes: A Molecular Dynamics Simulation Study. *J. Phys. Chem. B* **2015**, *119*, 3085-3096.
(87) Hou, T.; Yang, G.; Rajput, N. N.; Self, J.; Park, S.-W.; Nanda, J.; Persson, K. A. The influence of FEC on the solvation structure and reduction reaction of $LiPF_6$/EC electrolytes and its implication for solid electrolyte interphase formation. *Nano Energy*

2019, *64*, 103881.
(88) Dong, S.; Shi, L.; Geng, S.; Ning, Y.; Kang, C.; Zhang, Y.; Liu, Z.; Zhu, J.; Qiang, Z.; Zhou, L.; et al. Breaking Solvation Dominance Effect Enabled by Ion–Dipole Interaction Toward Long-Spanlife Silicon Oxide Anodes in Lithium-Ion Batteries. *Nano-Micro Lett.* **2024**, *17*, 95.
(89) Zeng, J.; Giese, T. J.; Ekesan, Ş.; York, D. M. Development of Range-Corrected Deep Learning Potentials for Fast, Accurate Quantum Mechanical/Molecular Mechanical Simulations of Chemical Reactions in Solution. *J. Chem. Theory Comput.* **2021**, *17*, 6993-7009.

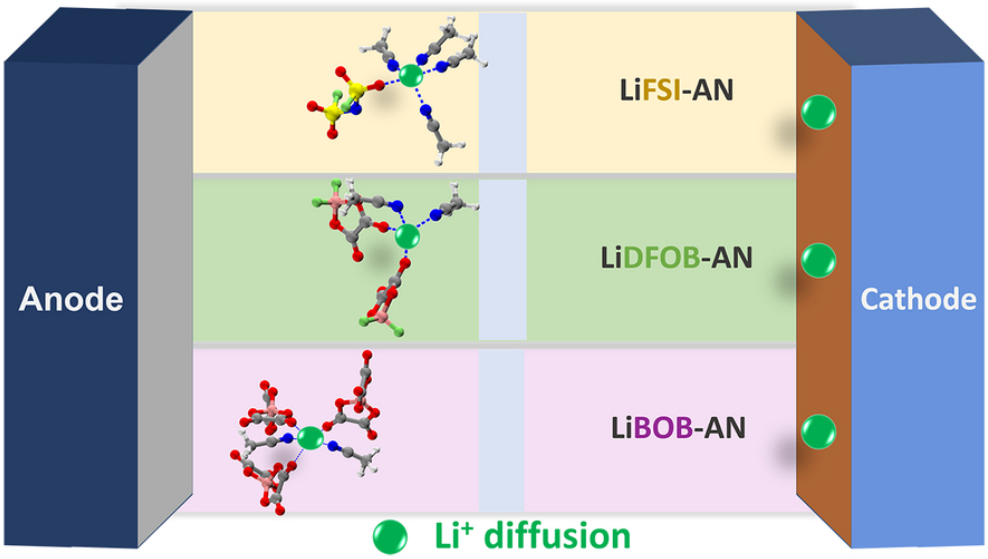

75x44mm (300 x 300 DPI)